On the Significance of Hydrate Formation/Dissociation during CO_2 Injection in Depleted Gas Reservoirs

Indina, V.; Fernandes, B. R.B.; Delshad, M.; Farajzadeh, R.; Sepehrnoori, K.

DOI
10.2118/218550-MS

Publication date
2024

Document Version
Final published version

Published in
SPE Conference at Oman Petroleum and Energy Show, 2024

Society of Petroleum Engineers

SPE-218550-MS

On the Significance of Hydrate Formation/Dissociation during CO_2 Injection in Depleted Gas Reservoirs

V. Indina, Hildebrand Department of Petroleum Engineering, University of Texas at Austin, Austin, Texas, USA; B. R. B. Fernandes, Center for Subsurface Energy and the Environment, University of Texas at Austin, Austin, Texas, USA; M. Delshad, Hildebrand Department of Petroleum Engineering, University of Texas at Austin, Austin, Texas, USA / Center for Subsurface Energy and the Environment, University of Texas at Austin, Austin, Texas, USA; R. Farajzadeh, Department of Geosciences and Engineering, Delft University of Technology, Delft, The Netherlands; K. Sepehrnoori, Hildebrand Department of Petroleum Engineering, University of Texas at Austin, Austin, Texas, USA

 DOI 10.2118/218550-MS

This paper was prepared for presentation at the SPE Conference at Oman Petroleum & Energy Show held in Muscat, Oman, 22 - 24 April 2024.

Abstract

The study aims to quantitatively assess the risk of hydrate formation within the porous formation and its consequences to injectivity during storage of CO_2 in depleted gas reservoirs considering low temperatures caused by the Joule Thomson (JT) effect and hydrate kinetics. The aim was to understand which mechanisms can mitigate or prevent the formation of hydrates. The key mechanisms we studied included water dry-out, heat exchange with surrounding rock formation, and capillary pressure. A compositional thermal reservoir simulator is used to model the fluid and heat flow of CO_2 through a reservoir initially composed of brine and methane. The simulator can model the formation and dissociation of both methane and CO_2 hydrates using kinetic reactions. This approach has the advantage of computing the amount of hydrate deposited and estimating its effects on the porosity and permeability alteration. Sensitivity analyses are also carried out to investigate the impact of different parameters and mechanisms on the deposition of hydrates and the injectivity of CO_2. Simulation results for a simplified model were verified with results from the literature. The key results of this work are: (1) The Joule-Thomson effect strongly depends on the reservoir permeability and initial pressure and could lead to the formation of hydrates within the porous media even when the injected CO_2 temperature was higher than the hydrate equilibrium temperature, (2) The heat gain from underburden and overburden rock formations could prevent hydrates formed at late time, (3) Permeability reduction increased the formation of hydrates due to an increased JT cooling, and (4) Water dry-out near the wellbore did not prevent hydrate formation. Finally, the role of capillary pressure was quite complex, where it reduced the formation of hydrates in certain cases and increased in other cases. Simulating this process with heat flow and hydrate reactions was also shown to present severe numerical issues. It was critical to select convergence criteria and linear system tolerances to avoid large material balance and numerical errors.

Keywords: Carbon Capture and Storage, CO_2 Hydrate, Depleted Gas Reservoirs, Thermal Reservoir Simulation, Joule-Thomson Effect

Introduction

Evidence suggests that the increase of greenhouse gas (GHG) concentrations in the atmosphere is the main cause of global warming and climate change (Rose et al. 2017). Underground storage of CO_2 is a promising method to mitigate global energy-related emissions (Bouzalakos and Mercedes 2010). Depleted natural gas reservoirs are identified as potential candidates for CO_2 storage because they provide a large storage capacity and already have part of the required infrastructure installed (Gauteplass et al. 2018; al Hagrey et al. 2014; Hoteit et al. 2019; Sun et al. 2016). However, injecting CO_2 at high pressure and low temperature, into a low-pressure depleted reservoir increases the risk of CO_2 hydrate and ice formation because of the Joule-Thompson (JT) cooling phenomena (Han et al. 2010; Oldenburg 2007; Zatsepina and Pooladi-Darvish 2012). Such thermophysical effects can significantly influence injectivity, which lead many researchers to conduct theoretical and experimental investigations to better understand this phenomenon and its possible risks (Wapperom et al. 2022; Zatsepina and Pooladi-Darvish 2012).

Aghajanloo et al. (2023) performed a comprehensive theoretical study about the impact of CO_2 hydrates on injectivity during CO_2 storage in depleted gas reservoirs. This study also discussed how pore size, rock minerals, water saturation, and impurities in the CO_2 stream affect hydrate formation in the reservoir. Moreover, this study found that capillary heterogeneity can cause capillary-driven backflow where water flows back to the direction of the injector. This phenomenon can impact the dynamic of water dry-out and hydrate formation during CO_2 injection.

Oldenburg (2007) investigated the magnitude of the Joule-Thomson cooling during CO_2 injection in Sacramento Valley, California. In their study, they investigated constant injection pressure scenarios and constant injection rates with low and high permeabilities. They used the TOUGH2/EOS7C simulator and validated their results with experimental data. They concluded that the JT cooling would not pose an issue for their field considering its permeability range, rate, and the heating of CO_2 through the pipes and wellbore. However, the authors do advise that care must be taken when injecting cryogenic CO_2. The results from Oldenburg (2007) were supported by the analytical solution developed by Mathias et al. (2010). However, the analytical solution considered three major assumptions: Constant thermophysical properties, single-phase flow, and steady-state pressure field.

Creusen (2018) did a comprehensive work focusing on the "near wellbore effect" during CO_2 sequestration in depleted gas reservoirs. They used numerical simulation to model the JT effect, the salt precipitation, and the hydrate formation using TOUGH2-ECO2MG and CMG-GEM. In the research, it was concluded that the CO_2 injection rate, injection temperature, reservoir permeability, and initial reservoir pressure are all critical parameters for the JT cooling and hydrate formation. They observed cooling as high as 15 to 20 °C in some cases due to the JT effect.

One of the first quantitative studies on the hydrate decomposition kinetics was done by Kim et al. (1987) for methane hydrates. The model presented by the authors considered a transient hydrate decomposition based on a fugacity gradient. In their model, the authors assumed the hydrate to be composed of spherical grains with a reactive layer. As the hydrate decomposes, a layer of gas ends up surrounding the hydrate grain. The triple point equilibrium fugacity is considered at the hydrate grain's surface. Englezos et al. (1987) presented a mechanistic model for the formation and growth of methane and ethane hydrates. The authors assumed the hydrates to be composed of spherical grains surrounded by an adsorption reactive layer which is surrounded by a stagnant liquid diffusion layer in which the gas diffuses from the fluid bulk to the hydrate reactive surface. The diffusion rate and adsorption rates are the same at steady-state, and the reaction is assumed to be of first order in the gas concentration due to excess water. This all leads to a model that relates the rate of hydrate formation to the difference between the dissolved gas fugacity

and the triple point equilibrium fugacity. This model is very similar to the one proposed by Kim et al. (1987) for dissolution, in the reverse direction, but the gas fugacity is replaced by the dissolved gas fugacity. Shindo et al. (Shindo et al. 1993a; Shindo et al. 1993b) proposed a kinetic model for the CO_2 hydrate formation. This model assumed that water would dissolve into liquid CO_2 and then react. A first-order reaction was considered but the water concentration in the liquid CO_2 was used instead of a fugacity. Ahmad et al. (2019) investigated the nucleation of CO_2 hydrate in hydrate-bearing formations for CCS with a non-isothermal approach that considered the time-dependent kinetics for hydrate growth. The authors assumed the hydrate formation to depend on CO_2 solubility. The authors observed pressure propagation delay with the reduction in permeability which resulted in less propagation of the CO_2 hydrate front. Furthermore, the authors observed the exothermic nature of the hydrate formation to slow the hydrate growth.

A sequence of series of developments in hydrate modeling and simulation was done by researchers from the Lawrence Berkeley National Laboratory. Moridis et al. (2008) presented the TOUGH+HYDRATE v1.0 simulator, developed for modeling the non-isothermal methane hydrate release from natural bearing formations. TOUGH+HYDRATE v1.0 could handle both equilibrium and kinetics hydrate reactions and used the model from Kim et al. (1987) for the kinetics case and is based on the work from Moridis et al. (1998). Later, TOUGH+HYDRATE v2.0 (Moridis et al. 2019) is a fully implicit non-isothermal compositional simulator and can describe all 15 possible thermodynamic states of the methane hydrate.

Coelho et al. (Coelho et al. 2021a; Coelho et al. 2021b) developed a compositional wellbore simulator for modeling the hydrate deposition risk assessment which could handle impurities, inhibitors, water evaporation, and the salinity effect. This was an equilibrium-based approach that used the chemical potential equality as proposed originally by van der Waals and Platteeuw (1958) and followed by other authors (Munck et al. 1988; Parrish and Prausnitz 1972). Coelho et al. (Coelho et al. 2021a; Coelho et al. 2021b) combined the IPHREEQc geochemistry module with a cubic EoS for modeling the phase equilibrium.

Yamada et al. (2024) developed a physics-based Machine Learning (ML) model to assess the risk of hydrates formation during CO_2 storage in depleted gas reservoirs. It is the first ML model applied to assess the risk of hydrate formation from injection conditions (injection rate and temperature) and reservoir properties (thickness, permeability, temperature, porosity, and water saturation). The authors observed deep neural network models to present the best predictive ability and observed injection rate, injection temperature, initial reservoir pressure, and reservoir permeability to have the highest impact on the risk of hydrate formation. However, the approach proposed by the authors could not quantify the amount of the formed hydrates.

In this paper, a thermal reservoir simulator was considered to assess the CO_2 hydrate risk and its consequences in a depleted gas reservoir considering the JT effect. This research is focused on modeling hydrate formation with a numerical simulator (CMG-STARS) using the formation/dissolution kinetic reactions to predict the hydrate formation and estimate the amount of hydrates formed and subsequent impact on injectivity. Sensitivity analysis of different parameters and key physical phenomena such as heat exchange with surrounding rock formation, capillary pressure, and permeability reduction are also considered.

Methodology

The CMG-STARS (version 2023.30) is used to simulate the Joule-Thomson cooling effect and hydrate formation in the depleted low-pressure reservoir model. Practically, we can calculate the temperature drop because of the cooling effect with the JT coefficient. The following defines the JT coefficient:

$$\mu_{JT} = \left(\frac{\partial T}{\partial P}\right)_H, \tag{1}$$

where T is temperature, P is the pressure, and H is the enthalpy. Eq. (1) indicates the dependency of JT coefficient on the fluid enthalpy. In STARS, the gas enthalpy is computed as

$$H_g = \sum_{i=1}^{n_c} y_i H_{gi}^{ideal} + H_g^{depart}, \tag{2}$$

where n_c is the number of components, y_i is the mole fraction of the *i-th* component in the gas phase, H_g is the gas phase total enthalpy, H_{gi}^{ideal} is the ideal gas enthalpy for component i, and H_g^{depart} is the gas phase departure enthalpy which is the deviation of the gas enthalpy from the ideal gas. The ideal gas enthalpy is computed as

$$H_{gi}^{ideal} = C_{pgi} T, \tag{3}$$

where C_{pgi} is the heat capacity for component i and is evaluated using the following correlation:

$$C_{pgi}^{ideal} = a_0 + a_1 T + a_2 T^2 + a_3 T^3 + a_4 T^4, \tag{4}$$

The departure enthalpy is computed from the corresponding states approach (Lee and Kesler 1975) as

$$\frac{H_g^{depart}}{RT_c} = \left[\frac{H_g^{depart}}{RT_c}\right]^{(0)} + \left(\frac{\omega}{\omega^{(r)}}\right)\left\{\left[\frac{H_g^{depart}}{RT_c}\right]^{(r)} - \left[\frac{H_g^{depart}}{RT_c}\right]^{(r)}\right\}, \tag{5}$$

where ω is the mixture acentric factor, T_c is the mixture critical pressure, R is the gas constant, the superscript (0) was used to denote the simple fluid departure enthalpy, and the superscript *(r)* denotes the reference fluid (n-Octane). Both departure enthalpy for the simple fluid and reference fluids are provided from the diagrams provided by Lee and Kesler (Lee and Kesler 1975). The mixture acentric factor is obtained from a mixing rule as

$$\omega = \sum_{i=1}^{n_c} x_i \omega_i, \tag{6}$$

where x_i is the mole fraction of component i in the phase, ω_i is the acentric factor of component i, and n_c is the number of components. The mixture critical temperature is also obtained from a mixing rule as

$$T_c = \frac{1}{8V_c} \sum_{j=1}^{n_c} \sum_{i=1}^{n_c} x_i x_j \left(V_{ci}^{1/3} + V_{cj}^{1/3}\right)^3 \sqrt{T_{ci} T_{cj}}, \tag{7}$$

where T_{ci} is the critical temperature from component i, V_{ci} is the critical volume from component i, and V_c is the mixture critical volume, also obtained from a mixing rule:

$$V_c = \frac{1}{8} \sum_{j=1}^{n_c} \sum_{i=1}^{n_c} x_i x_j \left(V_{ci}^{1/3} + V_{cj}^{1/3}\right)^3. \tag{8}$$

The hydrate kinetic model considered in STARS is based on Kim et al. (1987), originally proposed for hydrate dissociation and rewritten here as

$$-\frac{dn_h}{dt} = K_d A_h \left(f_h^* - f_h^g\right), \tag{9}$$

where n_h is the number of moles of hydrate of the gas component h, A_h is the surface area of the hydrate h which is assumed to consist of spheres, K_d is the dissociation rate constant, f_h^g is the fugacity of component h in the gas phase, f_h^* is the fugacity of component h in the gas-hydrate equilibrium, and t is the time.

In STARS, the model presented in Eq. (9) is modified by assuming that the fugacity coefficients are equal to one, the rate constant to follow the Arrhenius equation, and Raoult's law. Moreover, the same model is

considered for both hydrate formation and dissociation and is rewritten in terms of hydrate concentration. Therefore, Eq. (9) is rewritten as

$$\frac{dc_h}{dt} = \left(\frac{K_d^0 A_{hs}}{\rho_w \rho_h}\right)\left(\phi S_w \rho_w\right)\left(\phi S_h \rho_h\right)\left(y_h P_g\right)\left(1 - \frac{1}{K}\right) exp\left(-\frac{\Delta E_h}{RT}\right), \quad (10)$$

where c_h is the molar concentration of hydrate h, A_{hs} is the specific area of the hydrate h, K_d^0 is the intrinsic decomposition rate constant, ρ_w is the water density, ρ_h is the hydrate density of component h, φ is the porosity, S_w is the water saturation, S_h is the hydrate saturation of component h, y_h is the mole fraction of component h in the gas phase, P_g is the gas pressure, K is the equilibrium constant for the gas molecule considered, ΔE_h is the activation energy of the gas hydrate from component h, and T is the temperature. The K-values are defined by the hydrate equilibrium as the hydrate equilibrium pressure divided by the gas pressure (P_e/P_g) and are computed as

$$K = \left(\frac{r_1}{P_g} + r_2 P_g + r_3\right) exp\left(\frac{r_4}{T - r_5}\right), \quad (11)$$

where r_1, r_2, r_3, r_4, and r_5 are fitting parameters.

The gas phase density is calculated from the Redlich-Kwong cubic equation of state (Redlich and Kwong 1949) while the aqueous phase is assumed to be slightly compressible.

The gas phase viscosity is a function of temperature and composition only and is computed as

$$\mu_g = \frac{\sum_{i=1}^{n_c} y_i \sqrt{M_i}\, \mu_{gi}}{\sum_{i=1}^{n_c} y_i \sqrt{M_i}}, \quad (12)$$

where M_i is the molecular weight of component i, y_i is the mole fraction of component i in the gas phase, μ_{gi} is the viscosity of the pure component i computed as

$$\mu_{gi} = a_i T^{b_i}, \quad (13)$$

where a_i and b_i are fitting parameters.

The STARS default brine viscosity model was used.

Liquid CO_2 was observed in the reservoir conditions in our study. The simulator can model the liquid/gas equilibrium with K-values. However, severe numerical issues were observed during the phase transition, forcing us to consider the CO_2 gas and aqueous phases. While less accurate, we consider this to be a more conservative approach since the JT coefficient for the liquid CO_2 is significantly lower than that of the gas phase. In other words, more cooling is observed with the gas phase leading to more hydrates. We also observed anomalous behavior when the calculated gridblock temperature and pressure were close to the CO_2 critical point.

The K-values for water-CO_2 are obtained from Spycher et al. (2003) and for water-CH_4 are obtained from Sartini (2021).

Finally, permeability reduction can occur when hydrates and ice are formed as these will reduce porosity. The permeability change with porosity is modeled with a Kozeny-Carman relation (Moghanloo et al. 2018) as

$$k = k_0 \left(\frac{\phi}{\phi_0}\right)^{c_k} \left(\frac{1 - \phi_0}{1 - \phi}\right)^2, \quad (14)$$

where k is the permeability, k_0 is a reference permeability evaluated at a reference porosity φ_0 and c_k is an exponent that controls the permeability reduction.

Radial grids were used for performing the sensitivity studies. First, a 1D radial flow with a semi-open boundary for verification is presented with the solution obtained by Oldenburg (2007). Sensitivities using multilayer models are considered to investigate the effects of gravity and heterogeneity on the conditions for the formation of the hydrate.

Property and Parameters Survey and Validation

The first step is to validate the properties calculated with experimental data. This can help to be aware of any limitations imposed by these property models.

The K-values from Eq. (11) for both CO_2 and methane are shown at different temperatures in Fig. 1. The measured data used for calibration is water with zero salinity. While the latter assumption is unrealistic, it provides the worst-case scenario by making it more likely for hydrates to be formed. The calibration is provided by the CMG support team and the parameters are presented in Table 1.

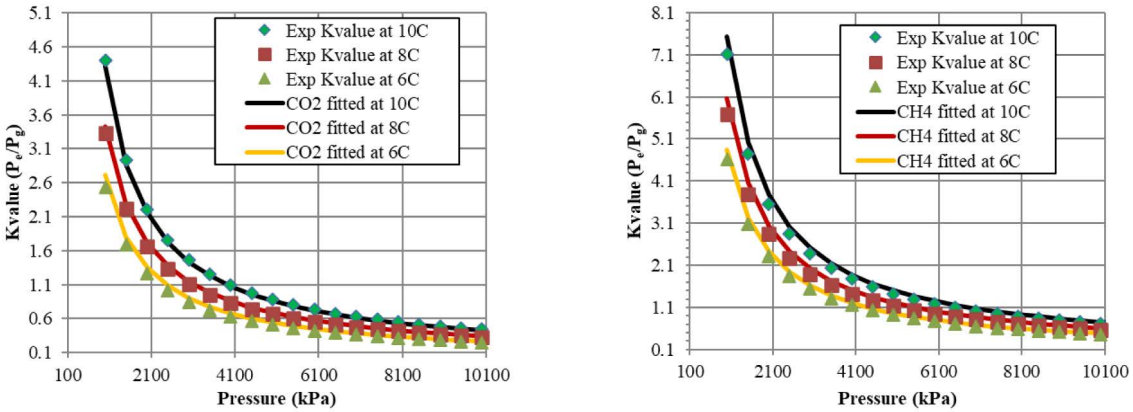

Figure 1—Calibrated hydrate K-values, in which P_e is the hydrate equilibrium pressure at a given temperature and P_g is the gas pressure. (a) CO_2; (b) methane.

Table 1—Calibrated coefficients for computing K-values performed by CMG support team.

Hydrate	r_1, kPa	r_2, kPa^{-1}	r_3	r_4, °C	r_5, °C
CO_2	1.7x10^9	0	0	−1485	−105.25
CH_4	1.6174x10^9	0	0	−1414.91	−105.25

Table 2 summarizes the thermophysical properties of the CO_2 and CH_4 hydrates, obtained by laboratory experiments or computational chemistry simulations, provided by different authors.

Table 2—General hydrate data.

Reference	Data type	Values
Aya et al. (1997)	CO_2 hydrate density	1090 - 1110 kg/m^3 at 30 MPa
Takeya et al. (2016)	CO_2 hydrate density	1105 kg/m^3 at 268K
Janicki et al. (2011)	CO_2 hydrate density	1106.805 kg/m^3
Sloan et al. (2007)	CH_4 hydrate density	900 kg/m^3
Janicki et al. (2011)	CH_4 hydrate density	919.94 kg/m^3
Mathews et al. (2020)	CO_2 hydrate heat capacity	148.86 J K^{-1} mol^{-1} (Calculated with density functional theory)

Reference	Data type	Values
Ning et al. (2015)	CO_2 hydrate heat capacity	0 - 74.43 J K^{-1} mol^{-1} (Molecular dynamics)
Handa (1986)	CH_4 hydrate heat capacity	107.7 - 257.6 J K^{-1} mol^{-1} from 85K - 270K
Nakagawa et al. (2008)	CH_4 hydrate heat capacity	164.38 - 197.26 J K^{-1} mol^{-1} - Cp = 1.159T+197.56

A review of the published experimental and theoretical values of the other parameters in the hydrate kinetic model is summarized in Table 3. Table 3 presents the activation energy for the hydrate dissolution obtained by different authors. Falenty et al. (2013) provided the activation energy for the CO_2 hydrate formation but it was not included to Table 3 since their model was based on aqueous concentration rather than fugacity. Similarly, Table 4 presents the reaction enthalpy obtained for CO_2 and CH_4 hydrates obtained by different authors.

Table 3—Hydrate activation energy.

Reference	Hydrate type	Values	Type
Clarke and Bishnoi (2004)	CO_2	102.88 kJ/mol	Dissociation
Kim et al. (1987)	CH_4	78.151±4.531 kJ/mol	Dissociation
Clarke and Bishnoi (2001)	CH_4	81kJ/mol	Dissociation

Table 4—Reaction enthalpy.

Reference	Hydrate type	Values	Type
Anderson (2003)	CO_2	63.6±1.8 kJ/mol - 57.7±1.8 kJ/mol	Dissociation
Larson (1955)	CO_2	60.2 kJ/mol	Dissociation
Bozzo et al. (1975)	CO_2	58.99 kJ/mol at 0°C, 58.16 kJ/mol at 10°C	Dissociation
Vlahakis et al. (1972)	CO_2	59.9 kJ/mol	Dissociation
Long (1994)	CO_2	73 kJ/mol	Dissociation
Kamath (1984)	CO_2	80.1 kJ/mol	Dissociation
Yoon et al. (2003)	CO_2	57.66 kJ/mol	Dissociation
Kang et al. (2001)	CO_2	65.22 kJ/mol	Dissociation
Gjerstad (2019)	CO_2	-67.79 kJ/mol - -58.55 kJ/mol	Formation
Janicki et al. (2011)	CO_2	65 kJ/mol	Dissociation
Gjerstad (2019)	CH_4	-57.07 kJ/mol - -48.76 kJ/mol	Formation
Anderson (2004)	CH_4	52.9 kJ/mol	Dissociation
de Roo et al. (1983)	CH_4	67.85 kJ/mol	Dissociation
Roberts et al. (1941)	CH_4	54.36 kJ/mol	Dissociation
Deaton and Frost Jr (1946)	CH_4	55.12 kJ/mol	Dissociation
McLeod and Campbell (1961)	CH_4	55.07 kJ/mol	Dissociation
Marshall et al. (1964)	CH_4	53.41 kJ/mol	Dissociation
Yoon et al. (2003)	CH_4	53.81 kJ/mol	Dissociation
Glew (2002)	CH_4	55.36 kJ/mol	Dissociation
Janicki et al. (2011)	CH_4	54 kJ/mol	Dissociation

The values of the intrinsic reaction constant and hydrate-specific area are nontrivial. The first reason is that different models use different assumptions and do not apply to the model considered in this study. Another issue is that the hydrate-specific area is not constant and changes over time during the dissolution or growth of the hydrate particles, while the model considered here requires a constant value. To overcome this issue, the assumption from Hong and Pooladi-Darvish (2005) was considered by taking the hydrate particle diameter to be constant and equal to 16 μm. This results in a specific area of 3.75×10^5 m^{-1}. The intrinsic reaction constant and its product by the specific area obtained by different authors in the literature are presented in Table 5. We only consider the intrinsic reaction constants for the papers with a reaction rate based on fugacity or pressure difference (dominated by the gas phase). It is important to mention that values for methane hydrate formation are presented by Englezos et al. (1987) but are not presented here because their model was based on aqueous concentration.

Table 5—Intrinsic Reaction Constant.

Reference	Hydrate type	K_d^0 (mol $m^{-2}kPa^{-1}d^{-1}$)	$K_d^0 A_{hs}$ (mol $m^{-3}kPa^{-1}d^{-1}$)	Type
Clarke and Bishnoi (2004)	CO_2	1.58×10^{16}	5.93×10^{21}	Dissociation
Kim et al. (1987)	CH_4	1.07×10^{13}	4.02×10^{18}	Dissociation
Clarke and Bishnoi (2001)	CH_4	3.11×10^{12}	1.17×10^{18}	Dissociation

The review of these data gives confidence in the values used in the simulations presented in this paper.

Finally, the gas viscosity parameters from Eq. (13) are $a_{CH_4} = 1.3 \times 10^{-4}$ cP and $b_{CH_4} = 0.7835$ for CH_4 and $a_{CO_2} = 1.048 \times 10^{-4}$ cP and $b_{CO_2} = 0.8784$ for CO_2. Again, the effect of pressure is not considered in Eq. (13). To evaluate the impact of pressure on viscosity, CO_2 and CH_4 gas viscosities are presented in Fig. 2 against experimental data (NIST) for different pressures within the range considered in this work. The error in viscosity is not significant where the maximum deviations are 6.55% and 6.60% for CH_4 and CO_2, respectively.

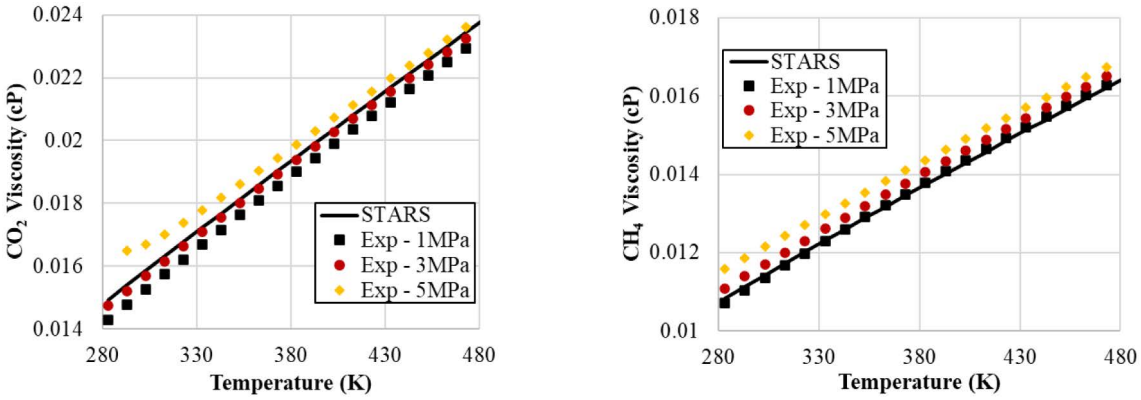

Figure 2—Comparison of calculated gas viscosity for different temperature and pressure values (points are experimental data and the black line is the STARS model). (a) CO_2; (b) CH_4.

Results

Case 1: Verification with Oldenburg (2007)

1D radial reservoir model was set up to verify the STARS capability of simulating the JT effect. The verification is performed by comparing the results from STARS with one case presented in Oldenburg

(2007). The data considered for this case is presented in Table 6 where CO_2 is injected at a constant rate while the CH_4 is produced through the outer boundary. A homogeneous permeability model is considered. Hydrates are not considered for this case. Figure 3 compares reservoir temperature, pressure, and the CO_2 overall composition profiles with those obtained by Oldenburg using TOUGH2 with similar results.

Table 6—Data for the verification case adapted from (Oldenburg 2007).

Parameter/Property	Value
Reservoir outer radius	1130 m
Initial reservoir temperature	45°C
Injection temperature	45°C
Initial water saturation	0.2
Initial gas composition	100% CH_4
Porosity	0.3
Permeability	5 mD
CO_2 injection rate	3 kg/s
CH_4 production rate	0.56 kg/s
Initial reservoir pressure	5 MPa

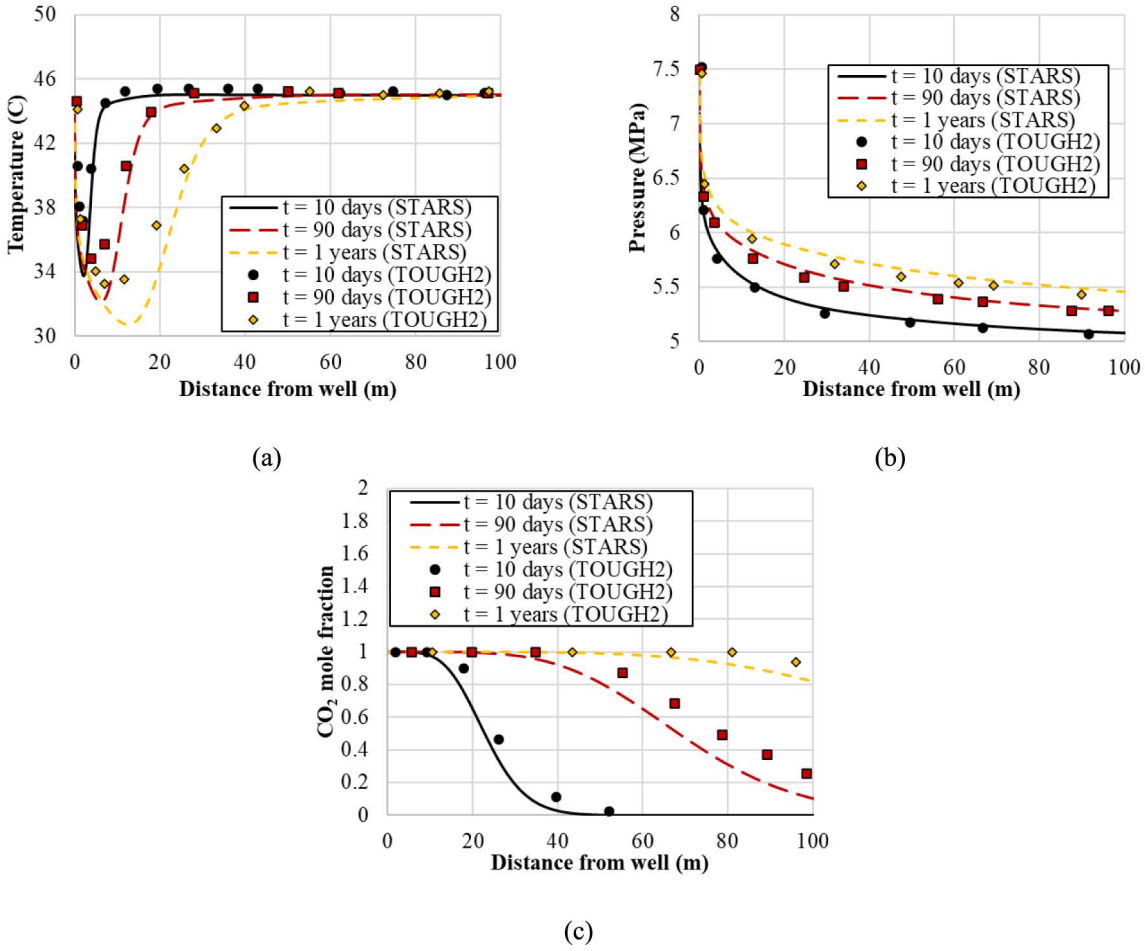

Figure 3—Comparison of time series of profiles in this study with Oldenburg (2007) (Symbols are from TOUGH2 and curves are from STARS). (a) Temperature; (b) Pressure; (c) CO_2 overall mole fraction.

Case 2: Hydrate study in a homogeneous reservoir

This case considers an infinite boundary homogenous reservoir modeled with a 1D radial grid with higher refinement near the wellbore. A sensitivity study was performed on this model to understand the impact of heat exchange with surrounding formations and permeability reduction. Reservoir temperature, pressure, CO_2 hydrate concentration, gas saturation, and porosity profiles are plotted to display the effects of heat exchange and permeability reduction. Unlike the previous case, there is no CH_4 production and pore volume multipliers are used in the external boundary to simulate an infinite boundary reservoir. Table 7 presents the reservoir data for this case. The heat exchange to underburden and overburden formations is computed with the boundary condition proposed by Vinsome and Westerveld (1980).

Table 7—Model data, reservoir, and fluid parameters for Case 2.

Parameter/Property	Value
Reservoir outer radius	1130 m
Reservoir initial temperature	45°C
Injection temperature	10°C
Water initial saturation	0.2
Porosity	0.3
Permeability	20 mD
Gas initial composition	100% CH_4
CO_2 injection rate	0.0946 MMTA (3 kg/s)
Reservoir initial pressure	3 MPa
Kv/Kh	0.1
Rock heat capacity	1000 kJ/(m^3 °C)
Rock heat conductivity	217 kJ/(m °C day)
Heat exchange to the surroundings	Sensitivity
Base/Cap rock heat capacity	1000 J/(kg °C)
Base/Cap rock heat conductivity	2.51 W/(m °C)
Permeability reduction	Sensitivity

Hydrate parameters used for Case 2 are based on the data presented in the previous section from the literature. Table 7 shows all hydrates parameters used for Case 2. These hydrates parameters are also used in the next sensitivity study named Case 3. Furthermore, the formation of hydrate is an exothermic process, thus releasing heat, while the dissociation is an endothermic process, thus taking heat from the surrounding. Finally, the formation of ice is modeled in STARS with latent heat (phase equilibrium) rather than a kinetics like approach.

First, a sensitivity for the heat exchange (hl) with the overburden and underburden formations is presented. Figure 4 presents a comparison of results obtained without and with heat exchange to the surrounding formations. Figure 4a presents the near wellbore temperature profiles at 10, 30, and 90 days of simulation. The heat exchange with surrounding formations creates a slight increase in temperature. As the time increases from 10 to 90 days, one can observe larger separation between the corresponding profiles. The temperature increase does not impact the pressure profiles in the near wellbore region (Fig. 4b). Additionally, there is a plateau in the temperature profile at 0°C after 90 days of simulation. This is caused by the formation of ice and how this is modeled by the numerical simulator. In STARS, ice is formed in a similar fashion to a pure component phase transition with a freezing temperature and latent

heat. Therefore, temperature can only go below freezing temperature after all water is converted into ice or hydrates. CO_2 hydrates were formed in both scenarios with a decrease in the amount of hydrates observed when heat exchange is considered (Fig.4c). The porosity profiles (Fig.4d) follow a similar behavior to the CO_2 hydrate concentration profiles. It can be observed from the temperature, CO_2 hydrate concentration, and porosity profiles that the effect of heat exchange with surrounding formations seems to intensify over time and cannot prevent hydrates from forming early in time. This would suggest that hydrates could be prevented by the heat exchange if hydrates were to be formed late in time.

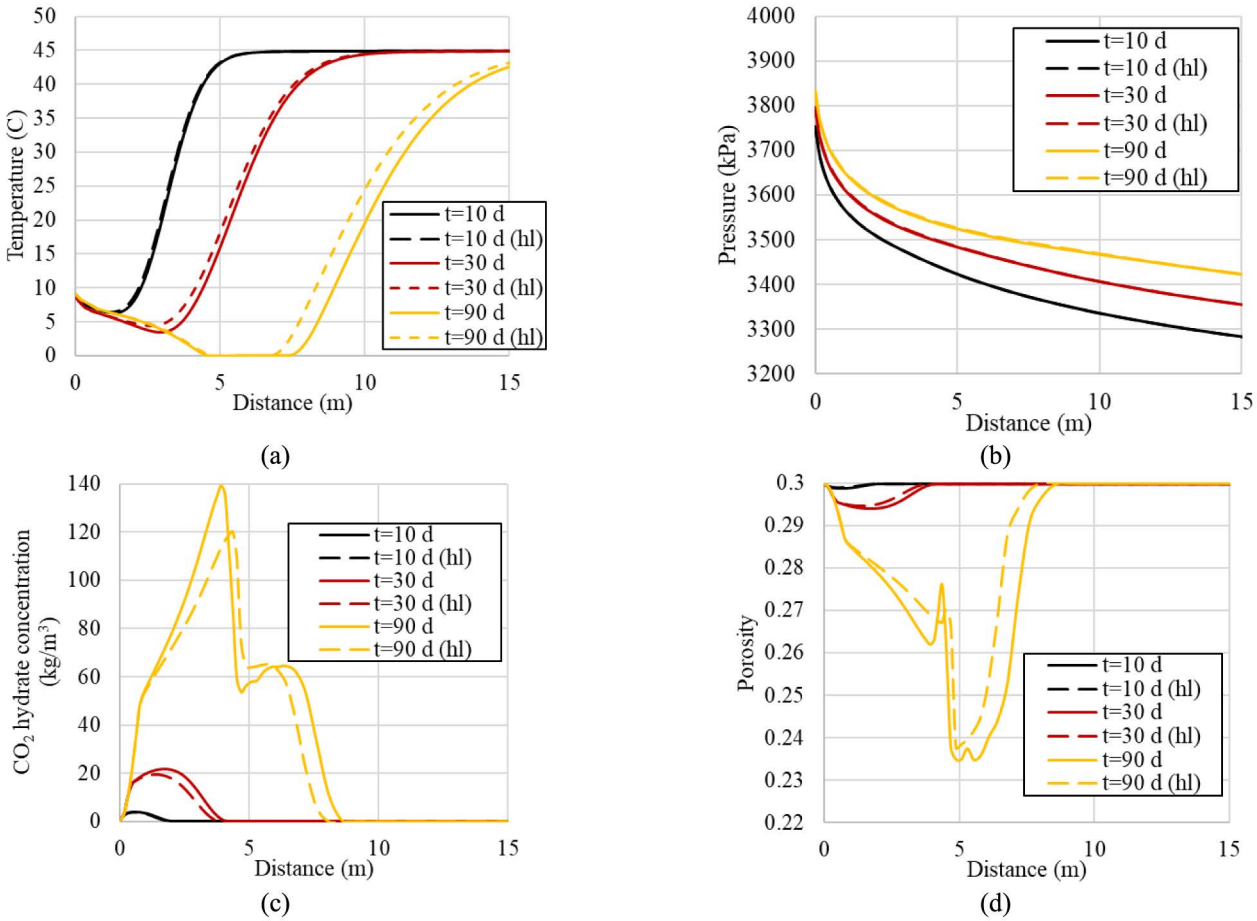

Figure 4—Time series of profiles for Case 2 with (dashed line) and without (solid line) heat exchange to the surrounding formations. (a) Temperature; (b) Pressure; (c) CO_2 hydrate concentration; (d) Porosity.

Next, a sensitivity to the permeability reduction is presented. The results of two simulations with and without permeability reduction are compared and different profiles are presented in Fig. 5. Both scenarios model heat exchange as presented before. The permeability reduction exponent (C_k) for the case with permeability reduction was 2 where an input value of 0 results in no permeability reduction. The near wellbore temperature profiles are presented in Fig. 5a for 10, 30, and 90 days of simulation. More cooling can be observed when permeability reduction is considered. As permeability reduces, the Joule-Thomson cooling increases because of the larger pressure drawdown. The increase in pressure can be observed in Fig. 5b especially at 90 days. As seen in Fig. 5c, CO_2 hydrates formed in the region with higher pressure values. The amount of CO_2 hydrates formed is also larger in the case with permeability reduction because of more significant JT cooling. Porosity profiles of the reservoir in Fig. 5d follow a similar trend as the CO_2 hydrate concentration profiles in Fig. 5c. From Figs. 5a-d, we can see that the effect of permeability reduction becomes more significant with time as more hydrate is formed. One important observation on

the porosity profile (Fig.5d) is the magnitude of porosity reduction when CO_2 hydrates formed. It is clearly seen in Fig. 5d that the maximum porosity reduction is around 20 percent. This reduction is in agreement with the amount of water originally in place. Hydrates and ice are only formed while liquid water is present in the porous media. Therefore, more water could lead to more porosity and permeability reduction.

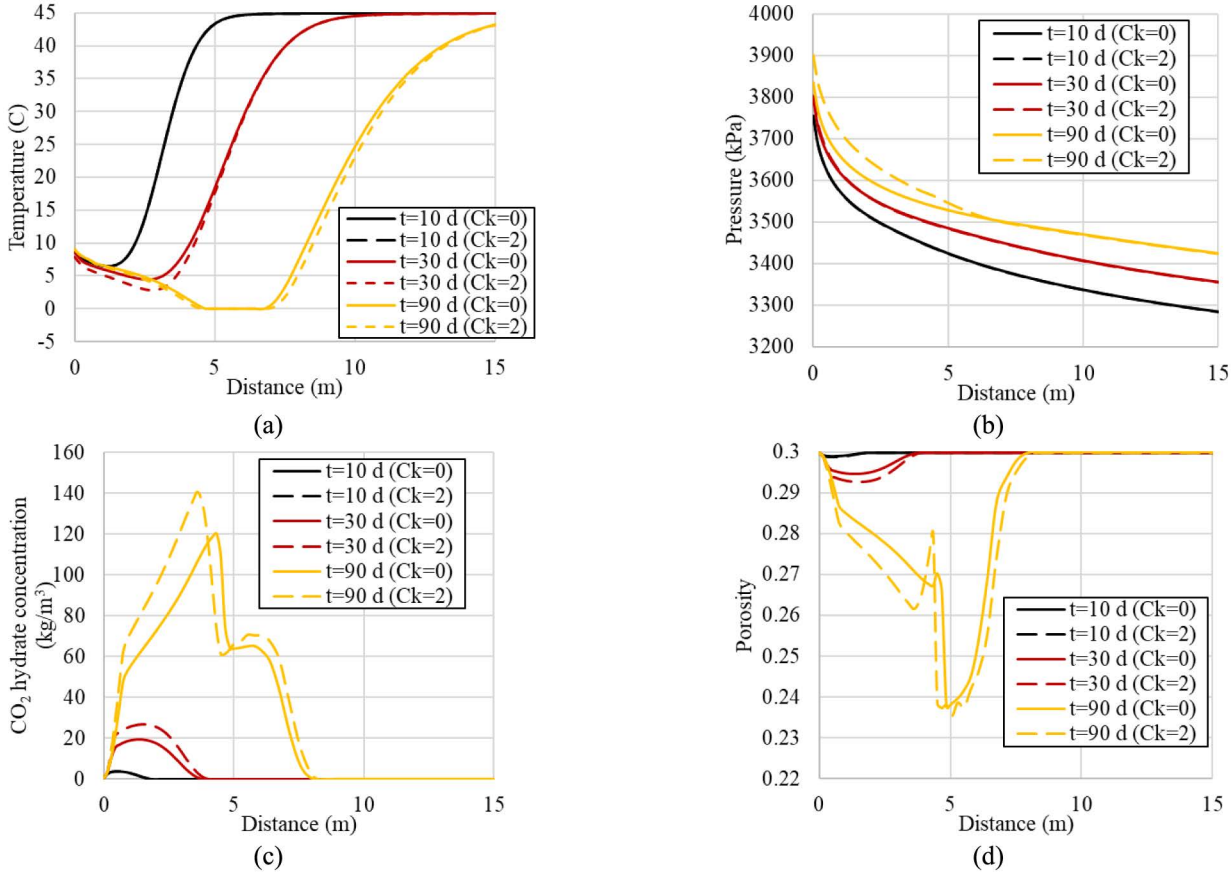

Figure 5—Time series of profiles for Case 2 with (dashed line) and without (solid line) modeling heat transfers from the surrounding formations. (a) Temperature; (b) Pressure; (c) CO_2 hydrate concentration; (d) Porosity.

Case 3: Layered radial reservoir

A reservoir model is built considering the upscaled data of a well log. A sensitivity analysis is performed to understand the different effects of the CO_2 injection in this formation. The reservoir model considers six layers and is assumed to be radially infinite using a pore volume multiplier at the outer boundary control volumes. A description of the reservoir model is presented in Fig. 6. The model data and sensitivity parameters are presented in Table 9. The parameters considered for sensitivity were the initial reservoir pressure, initial water saturation, injection rate, ratio between the horizontal to vertical permeability. The base model does not consider the effects of capillary pressure, permeability reduction, and heat exchange to surrounding formation and these are included as sensitivity scenarios. The hydrate kinetic model parameters are presented in Table 8.

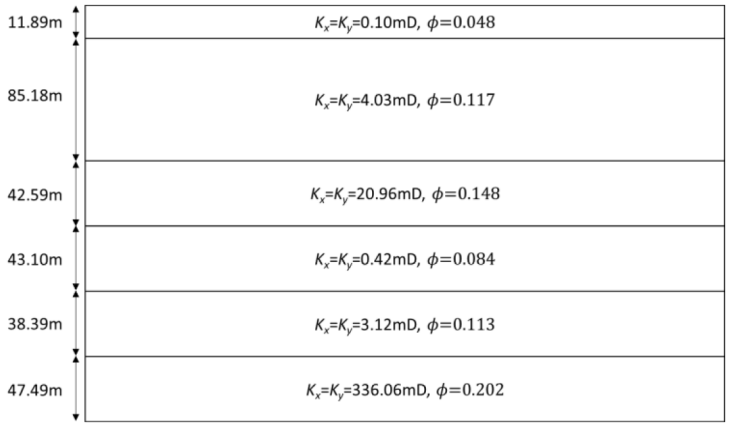

Figure 6—Reservoir layer properties for Case 3.

Table 8—Hydrate parameters for Cases 2 and 3.

Parameter/Property	CO_2	CH_4	Ice
Density, kg/m^3	1100	919.7	~916.89
Heat capacity, J mol^{-1} °C^{-1}	148.86	191.2	~37.12
Formation enthalpy, kJ/mol	60	55	-
Dissociation enthalpy, kJ/mol	-60	-55	-
Formation activation energy, kJ/mol	102	81	-
Dissociation activation energy, kJ/mol	102	81	-
Formation reaction constant product, ($K_d^0 A_{hs}$), mol m^{-3}kPa^{-1}d^{-1}	4.02x10^{18}	5.93 x10^{21}	-
Dissociation reaction constant product, ($K_d^0 A_{hs}$) mol m^{-3}kPa^{-1}d^{-1}	4.02x10^{18}	5.93 x10^{21}	-
Formation reaction frequency, $\left(\frac{K_d^0 A_{hs}}{\rho_w \rho_h}\right)$	3.65x10^{12}	6.45x10^{15}	-
Dissociation reaction frequency, $\left(\frac{K_d^0 A_{hs}}{\rho_w \rho_h}\right)$	3.65x10^{12}	6.45x10^{15}	-
Latent heat of fusion, kJ/mol	-	-	6.0

Table 9—Model data and sensitivity analysis parameter for Case 3.

Parameter/Property	Value	Sensitivity
Reservoir type	Radial infinite	-
Reservoir initial temperature	135°C	-
Injection temperature	10°C	15°C
Initial water saturation	0.2	0.15 and 0.3
Gas initial composition	100% CH_4	-
CO_2 injection rate	1 MMTA	0.5 and 2 MMTA
Initial reservoir pressure	2.5 MPa	1 and 4 MPa
Kv/Kh	0.1	0.5 and 1
Rock heat capacity	2600 kJ/(m^3 °C)	-
Heat conductivity	217 kJ/(m °C day)	-

Parameter/Property	Value	Sensitivity
Heat exchange to the surroundings	None	Include under and overburden
Capillary pressure	Not considered	J-function (Fig. 7)
Interfacial tension	0.03 N/m	-
Permeability reduction (C_k)	0	2

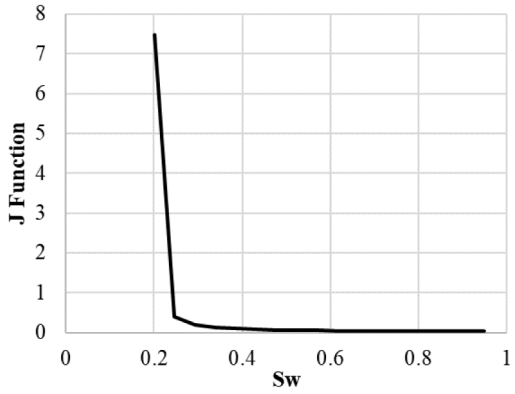

Figure 7—Leverett J function vs water saturation (S_w) considered for Case 3.

The near wellbore temperature field for the base case at 1 year of simulation is presented in Fig. 8a. The temperature changes are observed to be more significant in the higher permeability layers, with most of the temperature variation in the 6th layer (K_h=336.06 mD) followed by the 3rd layer (K_h=20.96 mD). This is a consequence of the higher flow rate through these layers which can be seen from the CO_2 front presented in Fig. 8d. Also, as CO_2 is injected into the formation, the water will slowly vaporize into the gas phase, causing a dry-out effect. For this case, this effect can be observed near the wellbore in Fig. 8b with water saturation being reduced to zero near the wellbore. A significant reduction in water saturation can also be observed a bit further from the well which coincides with reduction in porosity (Fig 8c) which is caused by the formation of ice and hydrates combined. While water dry-out could help mitigate the formation of ice and hydrates by reducing water content, it can be observed that the water drying front moves slower than the temperature cooling front. Therefore, hydrates and ice still form for this case. The temperature profiles for the 6th layer at 10 days, 90 days, and 1 year of simulation are presented in Fig. 9, from which it can be observed no significant difference from what would be observed from a 1D radial case such as the one presented in Case 2. However, a higher temperature near the wellbore can be observed at the 6th layer (about 12 °C) due to the higher pressure in that layer. On the other hand, the minimum temperature observed within the reservoir is as low as 0 °C after a year of injection with the formation of CO_2 hydrates and ice. The maximum distance of the temperature front from the wellbore after one year was 114.85 m.

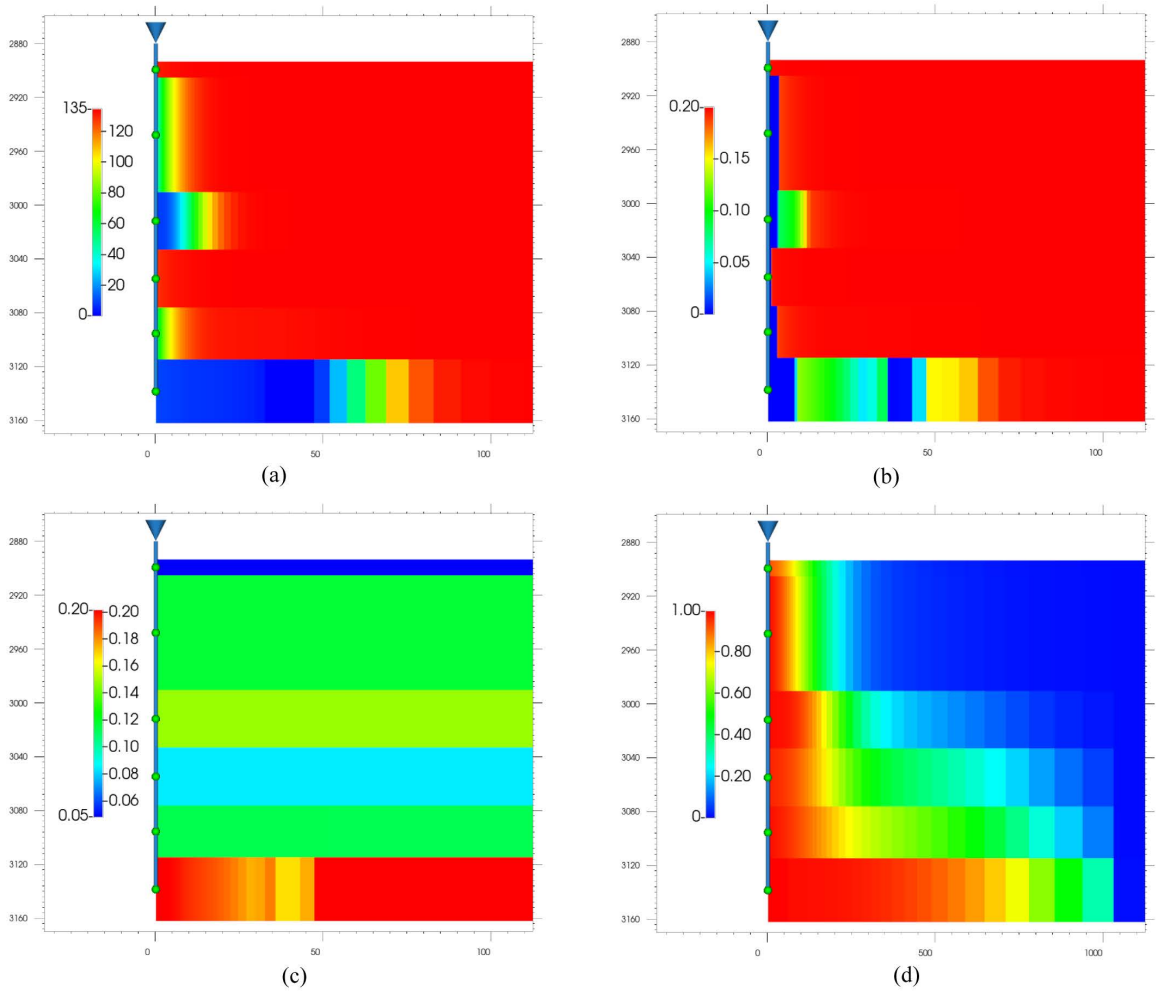

Figure 8—Cross-section plots at 1 year of simulation for Case 3 base scenario. (a) Temperature in °C; (b) water saturation; (c) porosity; (d) CO_2 mole fraction in the gas phase.

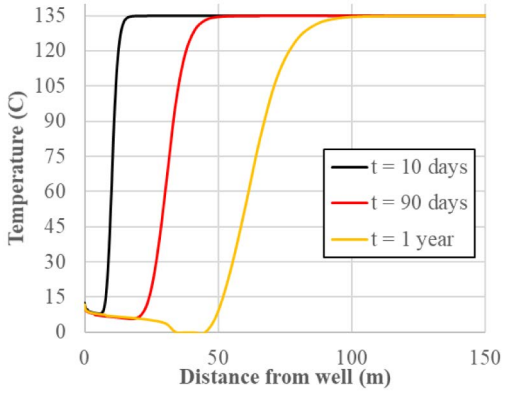

Figure 9—Temperature profiles (distance from the well) vs. time for the 6th layer from the base scenario for Case 3.

Most of the sensitivity scenarios considered resulted in the formation of hydrates as presented in Table 10. The only scenarios with no hydrate formation were the ones with lower injection rate and when heat exchange was considered.

Table 10—Hydrate risk sensitivity for Case 3 after 1 year of CO_2 injection at 10°C (shaded cells represent the cases in which hydrate formed).

Parameter/Property	Lower value	Higher value
CO_2 injection rate	0.5 MMTA	2 MMTA
Reservoir initial pressure	1 MPa	4 MPa
Kv/Kh	0.05	1
Water saturation (S_w)	0.15	0.3
Capillary pressure (Pc)	-	Included
Heat exchange to surrounding (HE)	-	Included
Permeability reduction (C_k)	-	2

While most cases present the formation of hydrates and even ice, the moment and behavior of the temperature over time is different among them. To summarize such differences, a tornado plot of changes in the minimum temperature is presented in Fig. 10 for 30, 90, 180, and 365 days of simulation. It is possible to observe that the minimum temperature of the base case decreases over time and eventually reaches the freezing temperature, which was also observed in Fig. 9. The inclusion of heat exchange mitigates the decrease in initial temperature over time. In fact, the minimum temperature stops decreasing after some time when heat exchange is considered (the minimum temperature at 180 and 365 days is very close). On the other hand, permeability reduction further reduced the JT cooling leading to freezing temperatures observed sooner than the base case scenario. Initial water saturation also had some impact on the temperature behavior. It was observed that higher water saturation resulted in lower temperatures while lower water saturation led to higher temperatures. The increase in water content leads can lead to more hydrate formation when CO_2 is injected. The first reason is that more water is available to be converted into hydrates. The second reason is that the CO_2 dry-out effect becomes less relevant as the water content increases and hydrates can form. Another reason observed in the simulations is the expansion of CO_2 when hydrates are formed which leads to more JT cooling. It is important to mention that the dry-out effect was not observed to prevent hydrates in any case. The impact of Kv/Kh is small with a maximum difference of 1°C. However, this could be due to the huge contrast between layers. It is also important to note that CO_2 flows favorably in the bottom layer due to methane's lower density, water being immobile, and the considerably higher permeability of the bottom layer. The inclusion of capillary pressure was observed to increase temperature only slightly. The initial reservoir pressure had a high impact on the temperature behavior. An increase in the initial pressure leads to a decrease in the JT cooling. However, it also leads to an increase in the hydrate equilibrium temperature and a further decrease in temperature once hydrates start forming. On the other hand, a lower initial pressure results in more JT cooling and a lower hydrate equilibrium temperature which can lead to hydrates forming at a later time, consistent with the behavior observed in Fig. 10. At 30 and 90 days of simulation, the amount of CO_2 hydrates is negligible for both 1MPa and 4MPa cases. At 180 days, a moderate amount of hydrates is present for the 4MPa scenario while the amount of hydrates is still negligible for the 1MPa scenario, which results in the inversion of the trend. At 365 days, both cases have a moderate amount of hydrates, but the 4MPa scenario has a much higher amount. Finally, the parameter with highest impact was the injection rate. As expected, increasing the injection rate results in a higher-pressure drawdown and more JT cooling while decreasing the injection rate results in lower pressure drawdown and less JT cooling.

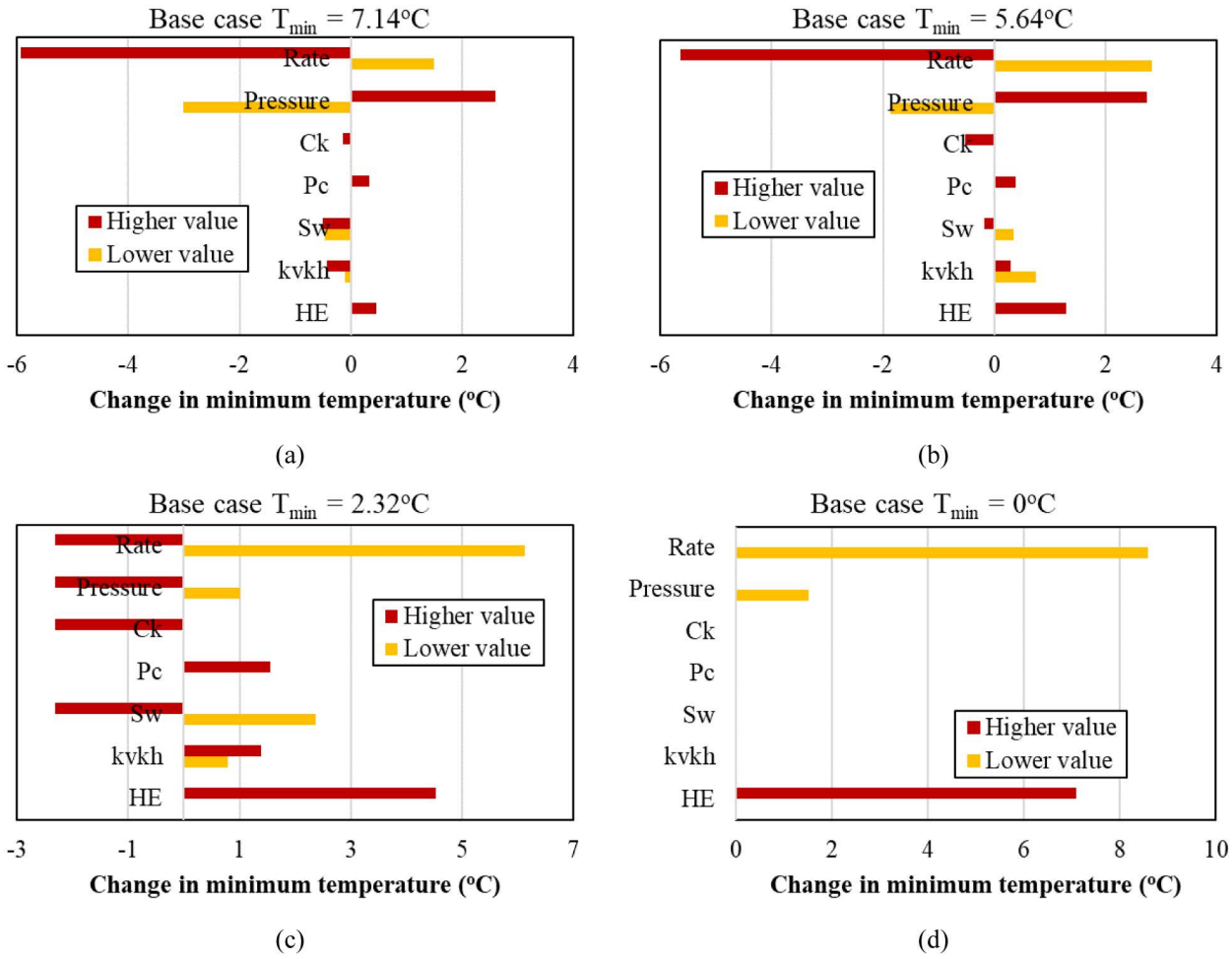

Figure 10—Tornado plot for the change in minimum temperature with respect to the base scenario for Case 3 (see Table 10). (a) 30 days; (b) 90 days; (c) 180 days; (d) 365 days.

Summary and Conclusions

A study of the JT cooling and hydrate formation during CO_2 injection in low-pressure gas reservoirs was presented. Results were verified with Oldenburg (2007) and a sensitivity study was performed. A summary of the insights observed in this study is presented below.

- The water dry-out zone was not deep enough into the reservoir to prevent hydrate formation since the cooling front was moving at a faster velocity.
- The cooling front moves much slower than the CO_2 front.
- Heat exchange with the underburden and overburden rock formations prevented the formation of hydrates for the multilayer case with a stabilization in the minimum temperature. However, hydrates still formed for the 1D case.
- The effect of the initial reservoir pressure was complex. Increase in pressure results in less JT cooling at an early time but leads to the formation of more hydrates and lower temperatures at later time. The opposite was observed when initial reservoir pressure is reduced.
- Minimum temperature in the reservoir was not sensitive to the ratio of vertical to horizontal permeabilities.
- Initial water saturation had an impact on the minimum reservoir temperature at later times. Higher water saturation led to more hydrates and more JT cooling.

- Permeability reduction amplified the JT cooling and increased the amount of hydrates formed. However, no plugging was observed by either by hydrates or ice in any of the cases presented.
- Injection rate has the most impact on the Joule-Thomson cooling and formation of hydrates. An increase in rates requires higher bottomhole well pressure which further increases the Joule-Thomson cooling effect.

Nomenclature

a Constants or fitting parameters
A Surface area, m^2
b Constants or fitting parameters
c Concentration, mol m^{-3}
c_p Specific heat capacity, J mol^{-1} K^{-1}
E Activation energy, kJ mol^{-1}
f Fugacity, Pa
H Enthalpy, kJ mol^{-1}
k Permeability, mD
K Equilibrium ratio
M Molecular weight, g mol^{-1}
n Number of moles, mol
P Pressure, Pa
r Constants or fitting parameters
R Gas constant, J mol^{-1} K^{-1}
S Saturation
t Time, sec
T Temperature, K
V Volume, m^3
x Liquid mole fraction

Greek

φ Porosity
μ Viscosity, cP
μ_{JT} Joule-Thomson coefficient
ω Mixture acentric factor
ρ Density, kg m^{-3}

Subscript

0 Reference condition
c Critical condition
g Gas phase
h Hydrate phase
i i-th component
j j-th component
s Specific hydrate surface area
w Water phase

Superscript

0 Simple fluid departure enthalpy

* Fugacity of component *h* in the gas-hydrate equilibrium
(*r*) Reference fluid
depart Enthalpy departure
ideal Ideal enthalpy
g Fugacity of component *h* in the gas phase

References

Aghajanloo M, Yan L, Berg S, Voskov D, Farajzadeh R. Impact of CO_2 Hydrates on Injectivity During CO_2 Storage in Depleted Gas Fields: A Literature Review. SSRN; 2023.

Ahmad S, Li Y, Li X, Xia W, Chen Z, Ullah N. 2019. Numerical analysis of CO_2 hydrate growth in a depleted natural gas hydrate formation with free water. *Greenhouse Gas Sci Technol* **9** (6): 1181–201.

Anderson GK. 2003. Enthalpy of dissociation and hydration number of carbon dioxide hydrate from the Clapeyron equation. *The Journal of Chemical Thermodynamics* **35** (7): 1171–83.

Anderson GK. 2004. Enthalpy of dissociation and hydration number of methane hydrate from the Clapeyron equation. *The Journal of Chemical Thermodynamics* **36** (12): 1119–27.

Aya I, Yamane K, Nariai H. 1997. Solubility of CO_2 and density of CO_2 hydrate at 30 MPa. *Energy* **22** (2–3): 263–71.

Bouzalakos S, Mercedes M. 2010. Overview of carbon dioxide (CO_2) capture and storage technology. In *Developments and Innovation in Carbon Dioxide (CO_2) Capture and Storage Technology*. ed. M. M. Maroto-Valer, Chap. 1, 1-24, Elsevier.

Bozzo AT, Hsiao-Sheng C, Kass JR, Barduhn AJ. 1975. The properties of the hydrates of chlorine and carbon dioxide. *Desalination* **16** (3): 303–20.

Clarke M, Bishnoi PR. 2001. Determination of the activation energy and intrinsic rate constant of methane gas hydrate decomposition. *Can. J. Chem. Eng*. **79** (1): 143–7.

Clarke MA, Bishnoi PR. 2004. Determination of the intrinsic rate constant and activation energy of CO_2 gas hydrate decomposition using in-situ particle size analysis. *Chemical Engineering Science* **59** (14): 2983–93.

Coelho FMC, Sepehrnoori K, Ezekoye OA. 2021a. A Coupled Hydrate and Compositional Wellbore Simulator: Understanding Hydrate Inhibition from Associated Brines in Oil and Gas Production. *SPE Production & Operations* **36** (04): 858–72.

Coelho FMC, Sepehrnoori K, Ezekoye OA. 2021b. Coupled geochemical and compositional wellbore simulators: A case study on scaling tendencies under water evaporation and CO_2 dissolution. *J. Pet. Sci. Eng*. **202**: 108569.

Cook J, Oreskes N, Doran PT, Anderegg WRL, Verheggen B, Maibach EW, et al. 2016. Consensus on consensus: a synthesis of consensus estimates on human-caused global warming. *Environ. Res. Lett*. **11** (4): 048002.

Creusen MCM. 2018. *Near wellbore effects induced by CO_2 injection and the influence on injectivity in depleted gas reservoirs*. Master Thesis, Delft University of Technology, Delft, Netherlands.

De Roo JL, Peters CJ, Lichtenthaler RN, Diepen GAM. 1983. Occurrence of methane hydrate in saturated and unsaturated solutions of sodium chloride and water in dependence of temperature and pressure. *AIChE J*. **29** (4): 651–7.

Deaton WM, Frost Jr EM. 1946. Gas Hydrates and their Relation to the Operation of Natural-Gas Pipe Lines. Report No.: BM-Mon-8, Helium Research Center, Bureau of Mines, Amarillo, TX, USA.

Englezos P, Kalogerakis N, Dholabhai PD, Bishnoi PR. 1987. Kinetics of formation of methane and ethane gas hydrates. *Chemical Engineering Science* **42** (11): 2647–58.

Falenty A, Salamatin AN, Kuhs WF. 2013. Kinetics of CO_2-Hydrate Formation from Ice Powders: Data Summary and Modeling Extended to Low Temperatures. *J. Phys. Chem. C*. **117** (16): 8443–57.

Gauteplass J, Almenningen S, Ersland G, Barth T. 2018. Hydrate seal formation during laboratory CO_2 injection in a cold aquifer. *International Journal of Greenhouse Gas Control* **78** :21–6.

Gjerstad PB. 2019. *Enthalpies of CH_4 and CO_2 Hydrate Formation and Dissociation Using Residual Thermodynamics*. Master's Thesis, University of Bergen; Bergen, Norway.

Glew DN. 2002. Aqueous nonelectrolyte solutions. Part XVIII. Equilibrium pressures of two methane hydrates with water. Formulae and dissociation thermo-dynamic functions for the structures I and II methane hydrates. *Can. J. Chem*. **80** (4): 418–39.

al Hagrey SA, Köhn D, Rabbel W. 2014. Geophysical assessments of renewable gas energy compressed in geologic pore storage reservoirs. *SpringerPlus* **3** (1): 267.

Han WS, Stillman GA, Lu M, Lu C, McPherson BJ, Park E. 2010. Evaluation of potential nonisothermal processes and heat transport during CO_2 sequestration. *J. Geophys. Res*. **115** (B7): B07209.

Handa YP. 1986. Compositions, enthalpies of dissociation, and heat capacities in the range 85 to 270 K for clathrate hydrates of methane, ethane, and propane, and enthalpy of dissociation of isobutane hydrate, as determined by a heat-flow calorimeter. *The Journal of Chemical Thermodynamics* **18** (10): 915–21.

Hong H, Pooladi-Darvish M. 2005. Numerical Study of Constant-Rate Gas Production from in Situ Gas Hydrate by Depressurization. In *Scientific Results from Malik 2002 Gas Hydrate Production Research Well Program, Mackenzie Delta, Northwest Territories, Canada*. ed SR Dallimore and TS Collett. Canada: Geological Survey of Canada.

Hoteit H, Fahs M, Soltanian MR. 2019. Assessment of CO_2 Injectivity During Sequestration in Depleted Gas Reservoirs. *Geosciences* **9** (5): 199.

Janicki G, Schlüter S, Hennig T, Lyko H, Deerberg G. 2011. Simulation of Methane Recovery from Gas Hydrates Combined with Storing Carbon Dioxide as Hydrates. *Journal of Geological Research*. **2011**: 1–15.

Kamath VA. 1984. *Study of Heat Transfer Characteristics During Dissociation of Gas Hydrates in Porous Media*. PhD Dissertation. Pittsburgh University; Pittsburgh, Pennsylvania, USA.

Kang S-P, Lee H, Ryu B-J. 2001. Enthalpies of dissociation of clathrate hydrates of carbon dioxide, nitrogen, (carbon dioxide+ nitrogen), and (carbon dioxide + nitrogen+ tetrahydrofuran). *The Journal of Chemical Thermodynamics* **33** (5): 513–21.

Kim HC, Bishnoi PR, Heidemann RA, Rizvi SSH. 1987. Kinetics of methane hydrate decomposition. *Chemical Engineering Science* **42** (7): 1645–53.

Larson SD. 1955. *Phase Studies of the Two-Component Carbon Dioxide-Water System Involving the Carbon Dioxide Hydrate*. PhD Dissertation. University of Illinois, Urbana, Illinois, USA.

Lee BI, Kesler MG. 1975. A generalized thermodynamic correlation based on three-parameter corresponding states. *AIChE J*. **21** (3): 510–27.

Long JP. 1994. *Gas Hydrate Formation Mechanism and Kinetic Inhibition*. PhD Dissertation. Colorado School of Mines, Denver, Colorado, USA.

Marshall DR, Saito S, Kobayashi R. 1964. Hydrates at high pressures: Part I. Methane-water, argon-water, and nitrogen-water systems. *AIChE J*. **10** (2): 202–5.

Mathews SL, Servio PD, Rey AD. 2020. Heat Capacity, Thermal Expansion Coefficient, and Grüneisen Parameter of CH_4, CO_2, and C_2H_6 Hydrates and Ice I_h via Density Functional Theory and Phonon Calculations. *Crystal Growth & Design* **20** (9): 5947–55.

Mathias SA, Gluyas JG, Oldenburg CM, Tsang C-F. 2010. Analytical solution for Joule–Thomson cooling during CO_2 geo-sequestration in depleted oil and gas reservoirs. *International Journal of Greenhouse Gas Control* **4** (5): 806–10.

McLeod HO, Campbell JM. 1961. Natural Gas Hydrates at Pressures to 10,000 psia. *Journal of Petroleum Technology* **13** (06): 590–4.

Moghanloo RG, Davudov D, Akita E. 2018. Formation Damage by Organic Deposition. In *Formation Damage During Improved Oil Recovery*. ed B Yuan and DA Wood, Chap. 6, p. 243–73, Elsevier.

Moridis GJ, Apps J, Pruess K, Myer LR. 1998. EOSHYDR: A TOUGH2 Module for CH_4-Hydrate Release and Flow in the Subsurface. Report No.: LBNL-42386. Lawrence Berkeley National Laboratory, Berkeley, CA, USA.

Moridis GJ, Kowalsky MB, Pruess K. 2008. TOUGH+HYDRATE v1.0 User's Manual: A Code for the Simulation of System Behavior in Hydrate bearing Geologic Media. Report No.: LBNL-149E. Lawrence Berkeley National Laboratory, Berkeley, CA, USA.

Moridis GJ, Queiruga AF, Reagan MT. 2019. Simulation of Gas Production from Multilayered Hydrate-Bearing Media with Fully Coupled Flow, Thermal, Chemical and Geomechanical Processes Using TOUGH + Millstone. Part 1: Numerical Modeling of Hydrates. *Transp Porous Med*. **128** (2): 405–30.

Munck J, Skjold-Jørgensen S, Rasmussen P. 1988. Computations of the formation of gas hydrates. *Chemical Engineering Science* **43** (10): 2661–72.

Nakagawa R, Hachikubo A, Shoji H. 2008. Dissociation and Specific Heats of Gas Hydrates Under Submarine and Sublacustrine Environments. Paper presented in the International Conference on Gas Hydrates (ICGH), Vancouver, British Columbia, Canada.

Ning FL, Glavatskiy K, Ji Z, Kjelstrup S, H. Vlugt TJ. 2015. Compressibility, thermal expansion coefficient and heat capacity of CH_4 and CO_2 hydrate mixtures using molecular dynamics simulations. *Phys. Chem. Chem. Phys*. **17** (4): 2869–83.

NIST. Thermophysical Properties of Fluid Systems. NIST Chemistry WebBook. Available from: https://webbook.nist.gov/chemistry/fluid/

Oldenburg CM. 2007. Joule-Thomson cooling due to CO2 injection into natural gas reservoirs. *Energy Conversion and Management* **48** (6): 1808–15.

Parrish WR, Prausnitz JM. 1972. Dissociation Pressures of Gas Hydrates Formed by Gas Mixtures. *Ind. Eng. Chem. Proc. Des. Dev*. **11** (1): 26–35.

Redlich Otto, Kwong JNS. 1949. On the Thermodynamics of Solutions. V. An Equation of State. Fugacities of Gaseous Solutions. *Chemical Reviews* **44** (1): 233–44.

Roberts OL, Brownscombe ER, Howe LS, Ramser H. 1941. Phase Diagrams of Methane and Ethane Hydrates. *Petr. Eng*. **12**.

Rose SK, Richels R, Blanford G, Rutherford T. 2017. The Paris Agreement and next steps in limiting global warming. *Climatic Change* **142** (1–2): 255–70.

Sartini M. 2021. *High Pressure Vapor-Liquid Equilibrium Measurements of Methane and Water Mixtures Using Nuclear Magnetic Resonance Spectroscopy*. Master's Thesis. Colorado State University, Fort Collins, Colorado, USA.

Shindo Y, Lund PC, Fujioka Y, Komiyama H. 1993a. Kinetics and mechanism of the formation of CO_2 hydrate. *Int. J. Chem. Kinet*. **25** (9): 777–82.

Shindo Y, Lund PC, Fujioka Y, Komiyama H. 1993b. Kinetics of formation of CO_2 hydrate. *Energy Conversion and Management* **34** (9–11): 1073–9.

Sloan Jr. ED, Koh CA, Koh CA. 2007. Clathrate Hydrates of Natural Gases. Third Edition. CRC Press.

Spycher N, Pruess K, Ennis-King J. 2003. CO_2-H_2O mixtures in the geological sequestration of CO_2. I. Assessment and calculation of mutual solubilities from 12 to 100°C and up to 600 bar. *Geochimica et Cosmochimica Acta* **67** (16): 3015–31.

Sun D, Ripmeester J, Englezos P. 2016. Phase Equilibria for the $CO_2/CH_4/N_2/H_2O$ System in the Hydrate Region under Conditions Relevant to Storage of CO_2 in Depleted Natural Gas Reservoirs. *J. Chem. Eng. Data* **61** (12): 4061–7.

Takeya S, Muromachi S, Yamamoto Y, Umeda H, Matsuo S. 2016. Preservation of CO_2 hydrate under different atmospheric conditions. *Fluid Phase Equilibria* **413**: 137–41.

Verheggen B, Strengers B, Cook J, van Dorland R, Vringer K, Peters J, et al. 2014. Scientists' Views about Attribution of Global Warming. Environ. *Sci. Technol*. **48** (16): 8963–71.

Vinsome PKW, Westerveld J. 1980. A Simple Method for Predicting Cap and Base Rock Heat Losses in Thermal Reservoir Simulators. *Journal of Canadian Petroleum Technology* **19** (3).

Vlahakis JG, Chen H-S, Suwandi MS, Barduhn AJ. 1972. The Growth Rate of Ice Crystals: The Properties of Carbon Dioxide Hydrate, a Review of Properties of 51 Gas Hydrates. Report No.: 986391. Sycaruse University Department of Chemical Engineering and Materials Science.

van der Waals JH, Platteeuw JC. 1958. Clathrate Solutions. In *Advances in Chemical Physics*. ed I Prigogine, p. 1-57. Hoboken, NJ, USA: John Wiley & Sons, Inc.

Wapperom M, Lyu X, Voskov D. 2022. Accurate Modeling of Near-Wellbore Effects Induced by Supercritical CO_2 Injection. Paper presented at the ECMOR 2022. The Hague, Netherlands.

Yamada K, Fernandes BRB, Kalamkar A, Jeon J, Delshad M, Farajzadeh R, et al. 2024. Development of a hydrate risk assessment tool based on machine learning for CO_2 storage in depleted gas reservoirs. *Fuel* **357**: 129670.

Yoon J-H, Yamamoto Y, Komai T, Haneda H, Kawamura T. 2003. Rigorous Approach to the Prediction of the Heat of Dissociation of Gas Hydrates. *Ind. Eng. Chem. Res*. **42** (5): 1111–4.

Zatsepina OYe, Pooladi-Darvish M. 2012. Storage of CO_2 as Hydrate in Depleted Gas Reservoirs. *SPE Reserv. Eval. Eng*. **15** (01): 98–108.